Simultaneous Multiscale Registration using Large Deformation Diffeomorphic Metric Mapping.

Laurent Risser, François-Xavier Vialard, Robin Wolz, Maria Murgasova, Darryl Holm, Daniel Rueckert

Abstract— **In the framework of Large Deformation Diffeomorphic Metric Mapping (LDDMM), we present a practical methodology to integrate prior knowledge about the registered shapes in the regularizing metric. We therefore discuss the link between the registration technique used to compare imaged organs and the physical meaning of its parametrization. Our interests are threefold: (1) We first present the notion of characteristic scale at which the features contained in two images are optimally compared. (2) With the increasing resolution of medical images, different biological phenomenons can be observed at several characteristic scales simultaneously. We therefore propose a methodology to compare such multiscale phenomenons. (3) In this context, we finally introduce a strategy to quantitatively measure the phenomenons occurring at each scale separately. After describing our methodology, we illustrate the meaning and influence of each of its parameters on phantom data. We then study its behavior on standard 3D MR longitudinal images out of the Alzheimer's Disease Neuroimaging Initiative (ADNI) study. We finally show its potential to quantify the anatomical evolution of the human brain from 3D MR longitudinal images of pre-term babies.**

Index Terms— **Diffeomorphic registration, multiscale, LDDMM, smoothing kernel, image comparison**

I. INTRODUCTION

NON-rigid image registration is of primary importance in medical image analysis. The reader unfamiliar with this field can find a recent and interesting comparison of standard non-rigid registration techniques in [1]. Importantly, these techniques can be applied to perform quantitative comparisons of the shapes represented in medical images. In this context, the underlying motivation of our work is to define pertinent and intuitive spatial regularizers when registering a source image I_S and a target image I_T according to the image features. In particular, we treat the notion of *characteristic scale* of the deformations, which refers here to the scale at which two shape features are optimally compared. For instance, to compare the cortical thickness in adult human brains $0.2-0.8$mm is a good range of characteristic scales. In hearts, to compare the size of the left atrial long axis between the end-diastole and end-systole characteristic scales of $5-20$mm is more pertinent. Practically, if the characteristic scale of the registration is s: (1) the deformations of features having a size smaller than s are considered as almost rigid and (2) the deformations of features having a scale larger than s may have no statistical meaning since very few spatial regularization constrain their deformations. Our key motivation is to compare quantitatively organs represented in 3D medical images. They may represent intra-subject longitudinal evolution of an organ, or a patient's organ relative to a healthy organ, represented by a standard shape. In both cases, the compared organs may contain anatomical structures having feature differences observed at several scales simultaneously. Importantly, due to the increasing resolution of medical images, such multi-scale structure variability can be fully imaged, as shown in section VI. This is also illustrated in Fig. 1, where a shape grows at large scale globally and also at small scale locally. The acquired images may also be subject to artifactual low frequency deformations at a scale different to the phenomenons of interest. It is therefore interesting to compare imaged shapes at several scales simultaneously and being able to quantify the deformations at a single scale among others. This is the problem we address in this paper.

Multi-scale properties in images can be characterized by using fractal or multi-fractal dimensions [2]–[4]. Another strategy to measure such properties is to use the power spectrum or the autocorrelation of the image [4], [5], which are directly related to Fourier transforms. Such measures are however global. The relation between scale and space in images has been an active field of research since early works in digital image analysis [6]. These issues have in particular been treated by the scale-space community [7]–[10] or by using wavelet decompositions [11], [12]. Our work differs from most of these studies since we focus on image comparisons and not the description of the images themselves. We therefore propose a practical paradigm to measure such variations in the framework of the Large Deformation Diffeomorphic Metric Mapping (LDDMM) [13]–[17], discussed in section II. We restrict our study to the simultaneous comparison of shapes at a limited number of user-defined characteristic scales. This gives therefore an intuitive control to the method parameterization and a physical meaning to the comparisons.

In practice, the prior knowledge on characteristic scales is integrated in the metric of the deformations which is a fundamental aspect of the LDDMM framework. The metric is indeed directly related to the smoothing kernel of the deformations that controls their spatial regularization as initially described in [18]. The idea of incorporating several characteristic scales in a metric is close to the idea underlying the strategy proposed in [19] which consists in registering images at several scales simultaneously. In the context of LDDMM, it is also related to the work of J. Glaunes where time-dependent kernels were used in the context of surface

---

Foundings

From the Institute for Mathematical Science, Imperial College, 53 Prince's Gate, SW7 2PG, London, UK (L.R., F.X.V., D.H.), Visual Information Processing research group, Imperial College, SW7 2BZ, London, UK (L.R., R.W., M.M., D.R.).

The authors thank Alain Trouvé, Xavier Pennec, Martins Bruveris and Franck Plouraboué for constructive discussions.

registration [20]. Note also that in [21], the authors contributed to the important topic of the choice of the metric: in particular, they introduced polyharmonic clamped-plate splines for the smoothing kernel and advocated their suitability for biological images. Finally, we emphasize that the role of the similarity measure is also another important topic of research. For instance [22], [23] make use of currents for the similarity measure. In this context, it would be worth studying the integration of some characteristic lengths within this similarity measure. Yet, our work is preliminary to such developments [24].

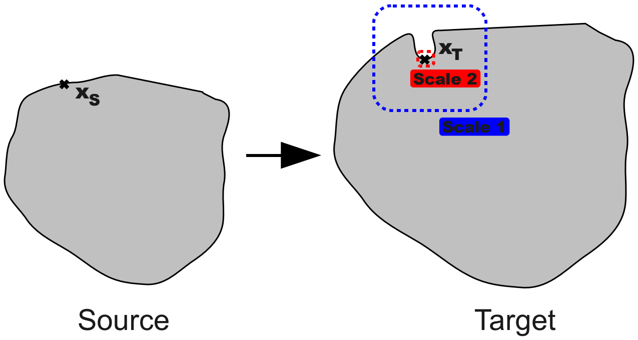

Fig. 1. Comparison of two shapes presenting differences at two characteristic scales simultaneously. At a large scale (scale 1), the shape grows relatively homogeneously while at a smaller scale (scale 2) a cavity locally differentiate the images. The diffeomorphism matching the point x_s of the source image to the point x_t of the target image ideally represents the simultaneous contribution of two clearly identified scales.

The paper is organized as follows. In section II, we present several techniques of diffeomorphic registration and explain our motivations to use the LDDMM formalism. A standard implementation of the LDDMM for 3D images [15] is then presented in section III and its multiscale extension introduced in section IV. In this context, we then propose in section V, a technique to quantify the deformations that occur at only one scale of interest among others from the initial image. These ideas were introduced in [25], [26] but the behavior of the methodology according to its parameters were briefly presented in the previous communications. In order to help the end-user to understand the phenomenons quantified at each scale, we then first propose in section V a new methodology to illustrate the deformations occurring at the different scales separately. In the section VI, we also describe four new tests that clarify the physical interpretation of the parameters and their optimal tuning. Again, it improves the usability of the method for the end-user. In particular, we illustrate the notion of characteristic scale which is at the heart of the paper. We also quantify the ability of our technique to detect feature differences at several scales simultaneously as a function of its parameters. Then, we compare its statistical power with a classical coarse to fine approach with no resampling of the images, on 3D MR images. Finally, we assess its potential to quantify the brain evolution in 3D images of pre-term babies.

II. CHOICE OF THE DIFFEOMORPHIC REGISTRATION FORMALISM

Diffeomorphic registration has gained a large interest in the last decade. Instead of encoding the deformation from a source image I_S to a target image I_T in displacement vector fields, it makes use of vector fields assimilated to velocity fields that deform the image points, considered as particles. In this context the deformation flow is the structure encoding the deformations. The benefit of such deformations is that it makes possible invertible large deformations that ensure the preservation of the objects topology. Spatial regularization on the velocity fields also enforces the smoothness of the deformations. Importantly, considering the flow of deformation to compare shapes, instead of the final deformation only, appears as an interesting option for quantitative shape comparisons.

In this paper, we used the Large Deformation Diffeomorphic Metric Mapping (LDDMM) framework [13]–[17] which foundations can be found in [27]. Here, the deformations are encoded in a time-dependent velocity field. A particularity of the LDDMM is that it is designed to estimate geodesics between the source and target images. This means that the optimal flow of deformation is the shortest path between the images according to a regularizing metric. In this case, the optimal path has shooting properties [28] from the velocity field at time 0 that can be used to statistically compare shapes [29]. A practical implementation of the LDDMM framework for image registration has been proposed in [15]. In [30], [31], the approach has been used to measure shape variations between segmented hearts, in order to highlight the structural remodeling of dyssynchronous failing hearts. In [32], [33] the LDDMM has been extended to vector- and tensor-valued images. Finally a symmetric extension has been proposed in [34]. However, although it was designed to allow large deformations, its practical use in real medical images is often limited to relatively small deformations. Note also that although we focus here on volumetric images comparisons most of the applications of the LDDMM framework were done on surfaces, like in [20], [35] for instance.

Alternative approaches have been proposed in the literature: For instance, a symmetric interpretation of [15] using cross correlation to measure the similarity between source and target images was proposed in [36]. This interpretation was used in [37] to measure the cortical grey matter thickness in segmented brain images. Another approach, allowing multimodal registration for atlas creation was proposed in [38]. More recently, [15] has been formulated as an optimal control problem in [39] leading to an improvement of the convergence speed and robustness. Approaches making use of the Navier-Stokes equation, have also been proposed [40], [41]. However, none of these alternatives has been explicitly designed to estimate geodesic transformations.

An important class of diffeomorphic registration techniques has also emerged with [42]. This paper indeed discusses the potential advantage of using exponential maps of constant velocity fields to model diffeomorphic deformations. The key advantage is the ability of exponential maps to model smooth, invertible and large deformations by using far less degrees of freedom than methods based on time-dependent velocity fields. These algorithms are then faster and require less memory than those using time dependent velocity fields. However, finding optimal and meaningful deformations using exponential maps still appears as an open field of research, particularly for large deformations. In [43] the authors use a formulation very similar to [15] but only update the velocity field encoding the flow of deformation at the final time of the deformation. Only relatively small deformations can therefore be estimated. In [44], exponential maps are composed iteratively to update a displacement field in an extension of Thirion's demons algorithm [45]. This leads to the fast estimation of smooth, invertible and potentially large deformations. Interestingly, an extension of this method where the total deformation is encoded in the exponential maps has also been proposed in [46]. Image comparisons can then be performed on the flow of deformation and not the displacement field only. Finally another important technique of diffeomorphic registration using exponential maps was proposed in [47]. Here the spatial regularization of the deformations is addressed in an elastic model. Again, it appears as a good alternative to the LDDMM formalism for many applications but it has not been designed to estimate geodesic transformations and may be limited to estimate large deformations.

Although interesting alternatives to the LDDMM exist, we developed our method using this framework. This is mainly due to its solid mathematical foundations which gives it a high potential to design new registration paradigms with a rich, intuitive and mathematically justified interpretation. It also appears as the most adapted approach to address organ feature comparisons with very large deformations. By discussing the choice of pertinent metrics for problem specific image comparisons, we hope to increase its usability for clinical applications.

III. LARGE DEFORMATION DIFFEOMORPHIC METRIC MAPPING

A. Standard registration algorithm

We give here an overview of the standard LDDMM registration algorithm [15]. Let I_S be a source image, defined on a spatial domain Ω, and registered on a target image I_T through the time-dependent diffeomorphic transformation ϕ_t of Ω, $t \in [0,1]$. This flow of deformation is defined by a time dependent velocity field v_t, $t \in [0,1]$ as follows (see also Fig. 2):

$$\begin{cases} \frac{\partial}{\partial_t}\phi_t = v_t(\phi_t), \quad t \in [0,1], \\ \\ \phi_0 = Id. \end{cases} \tag{1}$$

For notational convenience, we introduce $\phi_{t,s} \doteq \phi_s \circ \phi_t^{-1}$. We then use $I \circ \phi_{t,s}$ to denote the projection at time t of I taken at time s.

The registration problem then consists in finding the time dependent velocity field v_t that minimizes the sum of a similarity and a deformation energy:

$$E(v) = \int_0^1 \frac{1}{2}||v_t||_V^2 \mathrm{d}t + \frac{1}{2}||I_S \circ \phi_1^{-1} - I_T||_{L^2}^2 . \tag{2}$$

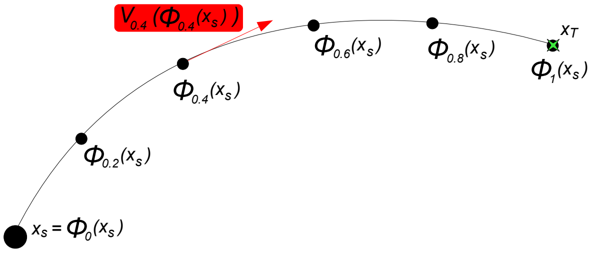

Fig. 2. Transportation of a point x_S of a source image I_S to match the point x_T of a target image I_T. The transportation is performed through ϕ_t which is defined by the time dependent velocity field v_t.

The second term measures the similarity between the deformed source image $I_S \circ \phi_1^{-1}$ and I_T. Here, the sum of squared differences between the image intensities is used. The energy of the deformation is computed as a special norm of v. The velocity field v is assumed to lie in $L^2([0,1], V)$, where the Hilbert space V is expressed by a smooth matrix valued kernel K describing the velocity fields that can be used for the registration. At time t, the norm can be computed by $||v_t||_V^2 =< \mathcal{F}(v_t)\mathcal{F}(K)^{-1}, \mathcal{F}(v_t) >_{L^2}$, where $\mathcal{F}(.)$ represents a Fourier transform. Even though there is a wide family of available kernels associated with V, most approaches use Gaussian kernels:

$$K(x) = (2\pi)^{-d/2}|\Sigma|^{-1/2} \exp\left(-\frac{1}{2}x^T\Sigma^{-1}x\right), \tag{3}$$

where Σ is the covariance matrix of the Gaussian kernel. In our work, we assume isotropic covariances, *i.e.* $\Sigma = \sigma Id_{\mathbb{R}^d}$, where the key parameter σ controls the level of spatial regularization of the deformations. The minimization algorithm is described hereafter. We denote $J_t^S = I_S \circ \phi_{t,0}$, $J_t^T = I_T \circ \phi_{t,1}$ and $|D\phi_{t,1}|$ the Jacobian of $\phi_{t,1}$ at time t. The minimization of the variational problem of eq. 2 is performed by using a steepest gradient descent approach. This involves the iterative use of the gradient of E in $L^2([0,1], V)$, $\forall t$:

$$\nabla_v E_t = v_t - K \star \left(|D\phi_{t,1}^v|\nabla J_t^S(J_t^S - J_t^T)\right), \tag{4}$$

where $\star$ denotes the convolution operator. The velocity field is then updated by computing:

$$v^{k+1} = v^k - \epsilon \nabla_{v_{t_j}^k} E, \tag{5}$$

where ϵ controls the step size during the gradient descent.

B. Extraction of the momentum maps

After convergence towards the minimum energy, the time dependent diffeomorphism resulting from the algorithm of [15] is a geodesic path in the group of diffeomorphisms for which the associated velocity field satisfies the Euler-Lagrange equation. It has therefore the interesting properties presented in section II which are computed from the initial momentum map P_0, a 3D scalar field encoding the 3D+t diffeomorphism in association with I_S and K. The initial momentum map can be retrieved from the initial velocity field by using $P_0 = Lv_0$, where L is the inverse operator of K. In practice, this calculation can be performed using Fourier transforms $\mathcal{F}(.)$ as follow:

$$\mathcal{F}(P_0) = \mathcal{F}(K)^{-1}\mathcal{F}(v_0)\,.$$

Note that this strategy may be sensitive to approximation errors, so P_0 may also be computed at every step of the gradient descent described in the previous subsection. More details are given in [48].

IV. FINE AND COARSE LDDMM

A. Introduction

In section I, we presented the notion of characteristic scale of the deformations that we also justify in the test of subsection VI-B. We also presented that, due to the increasing resolution of medical images, different biological phenomenons, occurring at several scales simultaneously, can be imaged. This opens new questions for the anatomical comparison of such phenomenons. In [25] we discussed that, to compare two images at several scales simultaneously in the LDDMM framework, computing the optimal flow of deformation at a large scale and then improving it at a small scale is not an appropriate strategy. The scale of the comparison is indeed entirely expressed by the metric of the final step of the registration. Hence, we propose a strategy to perform such comparisons with a physical meaning.

B. Registration paradigm

We define a registration paradigm in which the user empirically defines N characteristic scales σ_n at which the registered shapes have feature variations. This information is then incorporated into the metric underlying the kernel K presented in section III. Naturally, parameters a_n modeling the relations between the scales are also defined. If well defined, this incorporated knowledge leads to meaningful statistical comparisons of the images since problem-specific properties are integrated into the metric. Although this flexibility implies the definition of additional parameters, they are limited and can be tuned intuitively.

C. Sum of Gaussian kernels

To simultaneously perform the registration at several scales of interest, we propose to use kernels K that are the weighted sum of N Gaussian kernels K_n of different sizes:

$$\begin{aligned} K(x) &= \sum_{n=1}^{N} K_n(x) \\ &= \sum_{n=1}^{N} a_n (2\pi)^{-3/2} |\Sigma_n|^{-1/2} \exp\left(-\frac{1}{2}x^T\Sigma_n^{-1}x\right), \end{aligned} \tag{6}$$

where Σ_n and a_n are respectively the covariance matrix and the weight of the n^{th} Gaussian function. As in eq. 3, each Σ_n is only defined by a characteristic scale σ_n: $\Sigma_n = \sigma_n Id_{\mathbb{R}^d}$. Eq. 6 allows to construct a wide range of kernels with several scales of interest while preserving all the promising statistical properties of the LDDMM formalism. The meaning and practical tuning of the weights a_n is explained in the next subsection.

D. Definition of the weights

Our fine and coarse registration technique depends on a set of parameters a_n, $n \in [1, N]$ each of them controlling the weight of the deformations at scale n. A meaningful setting of the weights depends on: *(1) Representation and spatial organization of the structures*: A same structure can be encoded in various ways. For instance, it can be binarized or represented by a range of grey levels. The representation of the structures influences the a_n due to the similarity metric used in the Eq. 2. Similarly, the size and spatial relations between the structures influence naturally the choice of the a_n. *(2) Prior knowledge*: Prior knowledge about the amplitude of the structures displacement at each scale σ_n may be incorporated in a_n.

In [25] we proposed the following strategy to tune the weights a_n. We model each a_n as follows:

$$a_n = a'_n / g(K_n, I_S, I_T),$$

where $g(K_n, I_S, I_T)$ represents the typical amplitude of the updates of v_t in Eq. 8 when registering I_S to I_T at scale n. This value depends on the representation of the structures and their spatial organization so it cannot be analytically computed. An empirical technique to tune it is the following: for each K_n, the value of $g(K_n, I_S, I_T)$ can be estimated by observing the maximum update of the velocity field v in a pre-iteration of registration of I_S on I_T using only the kernel K_n with $a_n = 1$. The apparent weights a'_n, $n \in [1, N]$ provide an intuitive control of the amplitude of the displacements. When all values of a'_n are equal, the deformations of the main structures have a similar amplitude at each scale n. In practice, that would not be necessarily desired and the a'_n may then be different. This is explained in subsection VI-C on a synthetic example similar to the one described in Fig. 1. Subsections VI-D and VI-E also present the efficiency of this methodology on 3D medical images.

V. SEPARATING THE CONTRIBUTION OF EACH KERNEL

A. Introduction

In the last section, we proposed a registration paradigm that incorporates scale-related prior knowledge in order to find meaningful diffeomorphisms comparing complex biological shapes. In this section, our goal is to extract, from the optimal diffeomorphism ϕ, descriptors comparing the shapes at each characteristic scale n separately. For instance, in Fig. 1 the technique of section IV allows the estimation of a smooth diffeomorphism matching the source and target images accurately (see also subsection VI-C). We then aim to quantify the contribution of the scales 1 and 2 in ϕ separately. Importantly, our approach differs from a classical coarse to fine strategy in two ways: (1) We control the relation between different scales through the weights a_n. (2) More importantly, we quantify the deformations that occur at each single scale n from the source shape directly.

B. Optimization scheme

The formulation of the energy gradient given in Eq. 4, can be re-written to distinguish the contribution of each kernel K_n in ϕ. We associate a time dependent velocity field v_n with each kernel K_n. The energy gradient described in Eq. 4 is now:

$$\nabla_{v_n} E_t = v_{n,t} - K_n \star \left(|D\phi^v_{t,1}| \nabla J^S_t (J^S_t - J^T_t) \right), \quad \forall n, \tag{7}$$

and the velocity field update of Eq. 5 becomes:

$$v_n^{k+1} = v_n^k - \epsilon \nabla_{v^k_{n,t_j}} E, \quad \forall n. \tag{8}$$

Finally, similarly to Eq. 1, the diffeomorphism ϕ is computed by integrating the velocity fields v_n:

$$\begin{cases} \dfrac{\partial}{\partial t} \phi_t = \displaystyle\sum_{n=1}^{N} v_{n,t}(\phi_t), \\ \phi_0 = Id. \end{cases} \tag{9}$$

This formulation of the gradient descent is strictly equivalent to the original one and provides the same deformations. Using equations 7 and 8, the sum of the fields v_n is indeed equal to the total velocity field: $v = \sum_{n=1}^{N} v_n$. These properties are due to the construction of the kernel K as the sum of the kernels K_n. A key contribution in this section is the use we make of the velocity fields v_n as presented below.

C. Scale-dependent amplitude of the deformations

Our goal here is to quantify and visualize the deformations occurring at a scale of interest σ_n among others from the source image I_S directly. This is distinct to classic coarse to fine approaches where I_S is deformed first at large scale and then at finer and finer scales to match I_T. In this case scale-related descriptors comparing the images are indeed sequentially extracted from the successive deformations of I_S. To quantify the contribution of each kernel K_n in ϕ at a point x of I_S, we integrate in time the norm of each $v_{n,t}$ separately along the flow of deformation defined by ϕ_t, $t \in [0, 1]$ as follow:

$$AOD(x) = \int_0^1 |v_{n,t}(\phi_t \circ x)| \mathrm{d}t,$$

where AOD refers to the *amplitude of the deformations* along $\phi_t(x)$. In a Lagrangian representation of the deformation, *i.e.* by following the motion of each voxel, the AOD at scale σ_n will therefore integrate in time all the contributions of the kernel K_n. Obviously, using v_t instead of $v_{n,t}$ in this equation gives the length of the total deformation from x. Remark also that the sum of the AOD at all scales of interest may be different to the AOD of the total deformation since the different $v_{n,t}$ are not necessarily collinear. We show in section VI that the AOD is an interesting descriptor of the local deformations for shapes whose features exist across several scales. We also present in the next subsection a technique to illustrate the phenomenons quantified by the AOD.

D. Scale-dependent deformations of the source image

Let ϕ^n_t be the time-dependent deformations of Ω generated by the kernel K_n only. It can be computed as follows:

$$\begin{cases} \dfrac{\partial}{\partial_t} \phi^n_t = v_{n,t}(\phi_t), \quad \forall n \in \{1, \cdots, N\}, \\ \dfrac{\partial}{\partial_t} \phi_t = \displaystyle\sum_{n=1}^{N} v_{n,t}(\phi_t) = v_t(\phi_t), \\ \phi_0 = \phi^1_0 = \cdots = \phi^N_0 = Id. \end{cases}$$

Importantly, for all n, the velocity field is not integrated along the path of ϕ^n_t but the path of the general transformation ϕ_t. This formula is similar to the one of the AOD where the vectors $v_{n,t}$ are integrated instead of their norm. This is illustrated in Fig. 3 where a point x of Ω is transported along $\phi^n_t(x)$ according to the velocity field of v_n computed along $\phi_t(x)$.

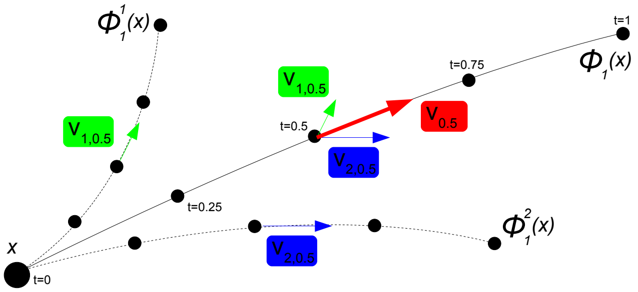

Fig. 3. Transportation of a point x along a path ϕ_t, $t \in [0, 1]$ (continuous line) computed using the velocity field v_t (red). The contributions $v_{1,t}$ (green) and $v_{2,t}$ (red) are distinguished here and the transportation of x along ϕ^1_t and ϕ^2_t shown (dashed lines).

We emphasize that each ϕ^n_t is not the deformation that would be computed if I_S was registered on I_T using the kernel K_n only. For instance, by referring again to Fig. 1, we want ϕ^2_t to reflect the creation of the cavity with a minor influence of the general shape growth. The registration with K_2 only would reflect the creation of the cavity and the general growth simultaneously.

Note also that even tough ϕ^n is smooth, it is not invertible in general. In practice, this property can be quickly checked by computing the determinant of the Jacobians $det(J)$. If $det(J(\phi_t(x))) > 0$, $\forall x \in \Omega$, the transformation is invertible. We always observed this property when the the characteristic scale σ_n was larger than the maximal amplitude of the deformations at the smaller scale σ_{n+1}. For example, in Fig. 1, the size of the cavity must be smaller than the characteristic scale σ_1. If this hypothesis is verified, the deformations that occur at scale σ_n therefore transport almost homogeneously those observed at scale σ_{n+1}. Importantly, this property was always respected in the tests of section VI and all the ϕ^n were invertible. To conclude, since the diffeomorphic properties of the deformations ϕ^n are not mathematically ensured, we propose to use them qualitatively only. As shown in section VI they are however a rich complement to illustrate and understand the phenomenons measured quantitatively by the AOD.

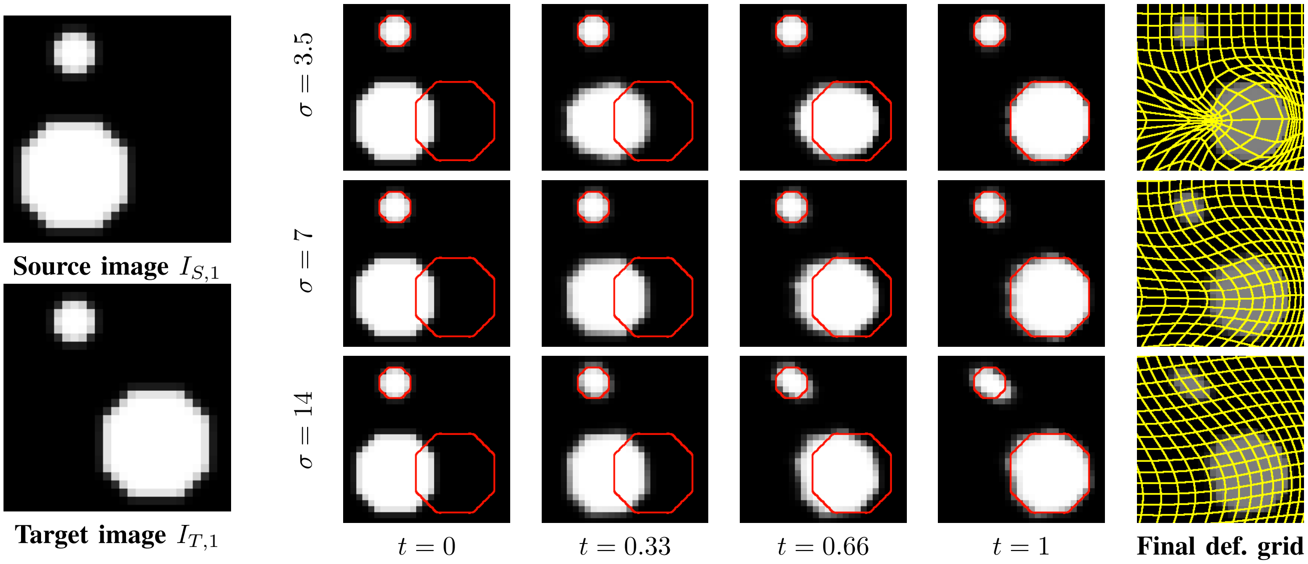

Fig. 4. Registration of the source image $I_{S,1}$ to the target image $I_{T,1}$ using isotropic Gaussian kernels of $\sigma = 3.5$ pixels **(top)**, $\sigma = 7$ pixels **(centre)** and $\sigma = 14$ pixels **(bottom)**. Diffeomorphic transformations of $I_{S,1}$ are shown at $t = 0$ (no deformation), $t = 0.33$, $t = 0.66$ and $t = 1$ (final deformation), where the red curves represent the shapes surface in $I_{T,1}$. On the right, the yellow grids represent uniform grids (step = 2 pixels) deformed at $t = 1$.

VI. TESTS AND DISCUSSION

A. Introduction

Our tests show first the influence of our model parameters. In subsection VI-B, we indeed give an empirical justification to the notion of characteristic scale and the influence of the weights a_n is discussed in subsection VI-C. We then show the usability and pertinence of using multi-scale kernels in 3D medical image comparisons through two examples. In subsection VI-D, our approach is quantitatively compared to a more classical coarse to fine strategy on standard 3D images out of the Alzheimer's Disease Neuroimaging Initiative (ADNI). We then use our method to measure the brain folding in MR cortical images of pre-term babies in subsection VI-E.

B. Characteristic scale of the deformations

In this section, we give an empirical and intuitive justification of the notion of characteristic scale. It is based on the test illustrated in Fig. 4: A source image $I_{S,1}$ is registered on a target image $I_{T,1}$. Both contain a large disc (radius = 7 pixels) that is translated to the right from $I_{S,1}$ to $I_{T,1}$. A smaller disc (radius = 2 pixels) is also relatively close to the large one in $I_{S,1}$ and remains at the same location in $I_{T,1}$. To compare $I_{S,1}$ and $I_{T,1}$, we then use three different isotropic Gaussian kernels referred here by $K_{3.5}$, K_7 and K_{14} with $\sigma = \{3.5, 7, 14\}$ voxels respectively.

In all cases, the matching of the large disc between $I_{S,1} \circ \phi_1^{-1}$ and $I_{T,1}$ is good, with slightly better results using $K_{3.5}$ than K_7 and K_{14}. Similarly, it appears that the higher σ, the higher the perturbation due to the registration of the large disc on the small disc. Indeed, the small disc is not deformed by using $K_{3.5}$ while it is slightly modified by using K_7 and strongly perturbed by using K_{14}. Following this observation, small kernels would be the best choice. However, this observation is counterbalanced by another one, observed in the deformation grids at $t = 1$. We described the deformation of the large circle from $I_{S,1}$ to $I_{T,1}$ as a translation and would ideally observe an almost rigid flow of deformation between these shapes. The grid deformed using $K_{3.5}$ between these shapes is strongly curved and is therefore far to represent an homogeneous translation. Quantitative comparisons performed using this deformation have not therefore the desired physical meaning. The deformations estimated using K_7 and K_{14} are not either exact translations but are clearly less curved. We conclude that among $K_{3.5}$, K_7 and K_{14}, K_7 represents the best balance between too few spatial regularization, leading to meaningless statistics, and too much spatial regularization perturbing the neighborhood of the structures of interest. In this example, we therefore consider 7 pixels, the size of σ, as a good characteristic scale. Note finally that non-Gaussian kernels could lead to better results in this particular example but for the sake of generality and simplicity, we restrict our study to isotropic Gaussian kernels.

C. Influence of the weights

In this second test, we present the influence of the weight when K is the sum of several kernels. Like in the example given in Fig. 1, the differences between the source image $I_{S,2}$ and the target image $I_{T,2}$ are observed at two different scales simultaneously. At a large scale the radius of the disc in $I_{S,2}$ grows by 4 pixels to match the one in $I_{T,2}$. At small scale, a small cavity of 5 pixels depth is also created in the disc of $I_{T,2}$. We build the kernel K as the sum of two isotropic Gaussian kernels K_1 and K_2 where $\sigma_1 = 10$ pixels and $\sigma_2 = 1$ pixels. The weights a_1 and a_2 are estimated using the technique of subsection IV-D, *i.e.* $a_1 = a'_1 / g(K_1, I_{S,2}, I_{T,2})$ and $a_2 = a'_2 / g(K_2, I_{S,2}, I_{T,2})$, where the values of g are automatically estimated. To present the influence of the apparent weights a'_1

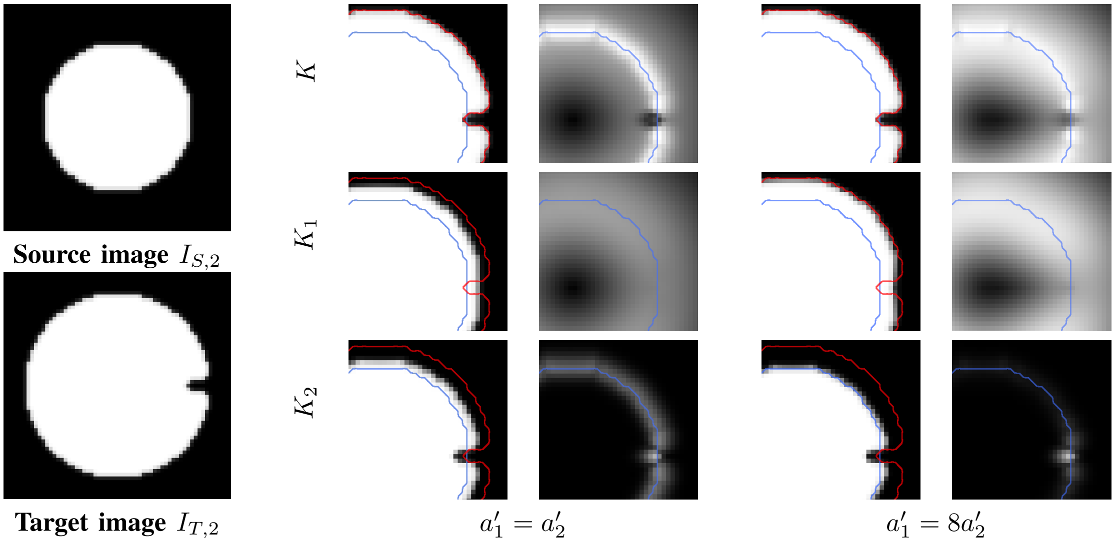

Fig. 5. Registration of the source image $I_{S,2}$ to the target image $I_{T,2}$ using the sum of isotropic Gaussian kernels K_1 and K_2 with $\sigma_1 = 10$ pixels and $\sigma_2 = 1$ pixel as kernel K. The results obtained using the apparent weights $a'_1 = a'_2$ **(left)** and $a'_1 = 8a'_2$ **(right)** are distinguished. We also distinguish the total deformation **(top)** and the contribution of K_1 **(centre)** and K_2 **(bottom)**. In every distinguished case, we show the final deformation **(left)** and the amplitude of deformations (AOD) **(right)**. For all AOD, black is a deformation of 0 pixels and white a deformation of 5 pixels. The blue curves represent the surface in $I_{S,2}$ and the red curves the surface in $I_{T,2}$.

and a'_2, we show in Fig. 5 the results obtained using $a'_1 = a'_2$ and $a'_1 = 8a'_2$. We present the total deformation due to K and the contributions of K_1 and K_2 distinguished using the technique of section V. Ideally, we would like to detect the radius growth at large scale only and the cavity deepening at small scale only. We then also present in Fig. 6 these estimated lengths compared with the expected ones as a function of a'_1/a'_2.

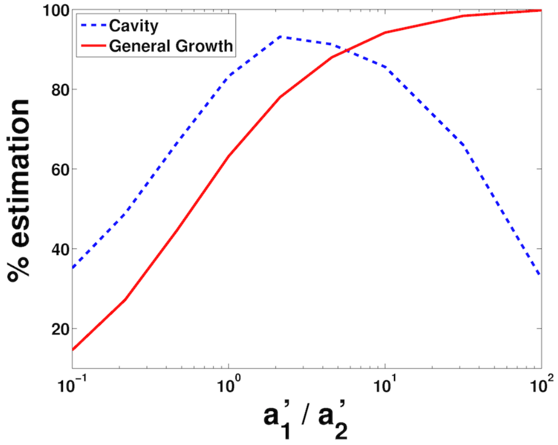

Fig. 6. Percentage of expected estimation of the disc radius growth (red continuous curve) and the cavity deepening (blue dashed curve), from $I_{S,2}$ to $I_{T,2}$, as a function of the ratio of the apparent weights a'_1 and a'_2. Results are given in percentage.

By observing the results of Fig. 5 and 6, three different behaviors of the algorithm can be distinguished as a function of a'_1/a'_2: (1) For $a'_1/a'_2 < 3$ the matching of $I_{S,2} \circ \phi_1^{-1}$ on $I_{T,2}$ is very accurate. This makes sense since the weight on the small scale σ_2 is clearly expressed in K. However the contribution of each scale separately is not as desired. The large scale σ_1 does not indeed express significantly the general disc growth ($< 80\%$). This can be observed in Fig. 5 where the general growth of the disc is clearly observed at large and small scale simultaneously when $a'_1 = a'_2$. As a result, the cavity deepening is not properly measured at small scale since this estimation is partially biased by the disc growth that, ideally, should not be detected at this scale. (2) For $3 \leq a'_1/a'_2 < 11$ the matching of $I_{S,2} \circ \phi_1^{-1}$ on $I_{T,2}$ is still very accurate. Moreover there is enough weight on the large scale to distinguish it from the influence of the small scale when estimating the general growth of the shape. In Fig. 6 we can observe that more than 80% of the general growth of the shape is detected at large scale. In Fig. 5 almost all the general shape growth is observed at large scale when $a'_1 = 8a'_2$. The estimation of the cavity deepening has therefore about 90% of accuracy compared with ideal results. (3) For $11 \leq a'_1/a'_2$ the separation of the large and small scales is clear. The disc growth at large scale is indeed estimated with more than 95% of accuracy. However the weight on the small scales is not large enough to match properly the shape details. The cavity deepening is therefore poorly estimated.

Our tests show that satisfactory results, *i.e.* more than 80% of accuracy compared with the expected results, are obtained for a large range of ratios: $3 \leq a'_1/a'_2 < 11$. For such configurations the deformations observed at large and the small simultaneously are then well separated. Note that the optimal separation is observed here for $a'_1 = 5a'_2$, with more than 90% of accuracy at both scales compared with our expectations. Importantly, we used a logarithmic scale on the a'_1/a'_2 axis of Fig. 6 and the curves are relatively smooth. This means that the results are stable for similar apparent weights. Additionally, note that the estimation of the cavity deepening would have been improved by using larger values of σ_1. Indeed, the higher σ_1, the smallest its ability to detect local phenomenons.

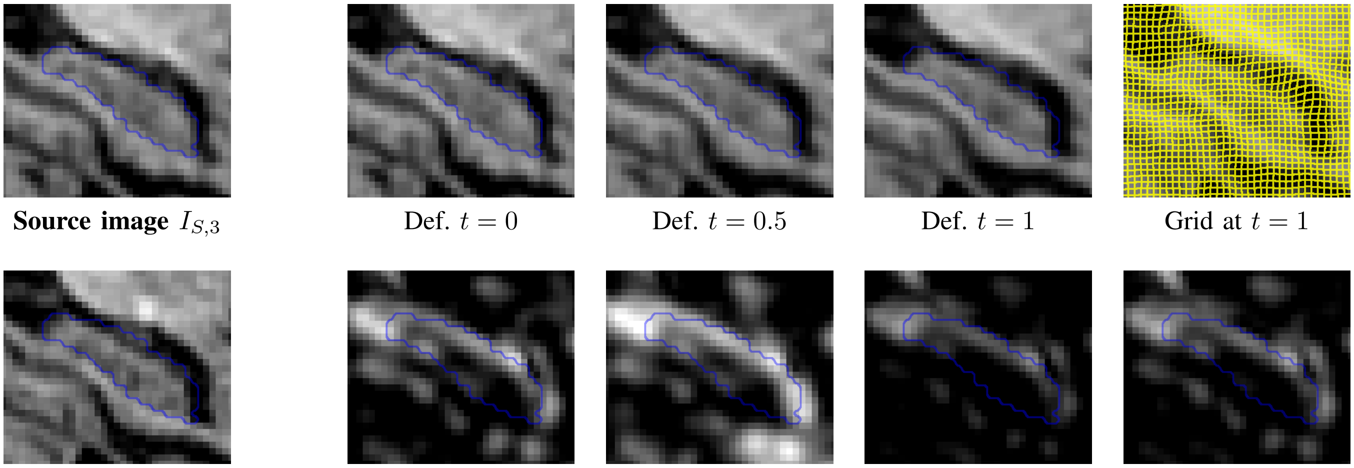
Source image $I_{S,3}$ Def. $t = 0$ Def. $t = 0.5$ Def. $t = 1$ Grid at $t = 1$

Target image $I_{T,3}$ AOD SK$_2$ AOD SK$_1$ AOD LSK$_1$ AOD SGK2$_1$

Fig. 7. Registration of the 3D MR source image $I_{S,3}$ (baseline) to the target image $I_{T,3}$ (follow-up) using several strategies. The blue curve represents the baseline hippocampal surface. **(Top)** Transformations of $I_{S,3}$ are shown at $t = 0$ (no deformation), $t = 0.5$ and $t = 1$ (final deformation) using the strategy SGK$_1$. The deformation grid at $t = 1$ with 1 mm of step size is presented on the right. **(Bottom)** Amplitude of the deformation flow using the strategies SK$_2$, SK$_1$, LSK$_1$ and SGK2$_1$. The brighter a point the larger the path of the deformation. The grey levels are linearly sampled between 0.2 and 1.2mm.

It is interesting to remark that the separation of phenomenons observed at different scales, performed here simultaneously, is classically done sequentially in coarse to fine techniques. Moreover, for any ratio a'_1/a'_2, the expected global growth and local deepening were simultaneously measured with more than 95% of accuracy. It is then natural to wonder what would be the behavior of a sequential approach for this kind of task. Obviously, the deformations at large scale would be perturbed by those at small scale and then those at small scale biased by the lack of accuracy of the deformation at large scale. The issues are then similar. To clarify this point, we then compare in the next subsection the statistical power of our coarse and fine registration technique with a coarse to fine one on standard 3D MR images to distinguish two groups of imaged organs.

D. Quantitative assessment on MR images

Our aim here is to assess, in MR images, the ability of our method to detect deformations at a scale of interest when other deformations also occur at a larger scale of interest. To do so, we downloaded 60 MR brain image pairs taken at baseline and after 24 months follow-up from the Alzheimer's Disease Neuroimaging Initiative (ADNI) study [49]. A total of 30 image pairs were acquired from patients with Alzheimer's disease **(AD)** and 30 others from healthy age-matched controls **(CN)**. All T1-weighted 1.5T MR-images were pre-processed using the standard ADNI pipeline. Then, we compared the statistical power of several strategies to discriminate (AD) and (CN) by measuring the atrophy of the hippocampus.

First, we distinguished two strategies to linearly align the baseline and follow-up images: **(S$_1$)** All images were aligned with the MNI152 brain template using affine registration. **(S$_2$)** Each follow-up image was aligned with the corresponding baseline image using affine registration. The alignment between the baseline and follow-up images is clearly more accurate using (S$_2$) than (S$_1$). The image pairs aligned using (S$_2$) almost only present differences due to the atrophy of the tissues, while those aligned using (S$_1$) also present differences due to an inaccurate linear alignment.

TABLE I

P-VALUES OF MANN-WHITNEY TESTS DISCRIMINATING AD AND CN USING AVERAGE AND MAXIMAL AOD IN EACH SUBJECT HIPPOCAMPAL SURFACE. THE LOWER THE P-VALUE, THE CLEARER THE DISTINCTION.

	Max AOD			Average AOD		
	a. AD	a. CN	P-val.	a. AD	a. CN	P-val.
SK$_2$	1.1	0.66	3.5e-07	0.46	0.22	1.6e-08
SK$_1$	1.1	0.74	2.5e-06	0.48	0.26	1.2e-06
LSK$_1$	0.96	0.48	1.1e-07	0.32	0.15	2.2e-07
SGK2$_1$	0.98	0.53	7.9e-09	0.34	0.17	3.2e-09

Either for (S$_1$) and (S$_2$), we then extracted regions of interest of 128^3 voxels around the hippocampus in all images. For (S$_1$), we then registered all the baseline and follow-up images using several strategies: **(SK$_1$)** Using directly a small characteristic scale $\sigma_2 = 1.5$mm adapted to the measure of the hippocampal atrophy. **(LSK$_1$)** Using the same characteristic scale σ_2, but after a first step of registration at large scale. The optimal deformations at large scale were obtained using $\sigma_1 = 15$mm and were composed with those at small scale so that the baseline images are only resampled one time to match the follow-up images (cf. [50]). This strategy corresponds to a coarse to fine approach. **(SGK$_1$)** Using directly the sum of two kernels of characteristic scales $\sigma_1 = 15$mm and $\sigma_2 = 1.5$mm with apparent weights $a'_2 = 7a'_1$ and the average g_1 and g_2 in the 60 image pairs. **(SGK2$_1$)** Using the same kernel as in (SGK$_1$) and isolating the contribution of the kernel at small scale. For (S$_2$), we finally registered the images by using only **(SK$_2$)** the small kernel of characteristic size $\sigma_2 = 1.5$mm. Typical results are illustrated in Fig. 7.

We compared the hippocampal temporal changes using several descriptors by automatically segmenting the hippocampus in all baseline images and transforming these volumes using the flow of deformations resulting from the registration of the grey level images. We measured the amplitude of the deformation (AOD) from each point x of the baseline images. For each subject, we therefore computed the average and maximum AOD from the hippocampal surface. These values, averaged in the groups AD and CN are given in millimeters in the (a. AD) and (a. CN) columns of table I. Group-dependent P-values of non-parametric Mann-Whitney tests between the groups AD and CN, which measure the discriminative power of each descriptor, were then computed. Note that prior to these tests, the AOD have been non-dimensionalized by the cubic root of the hippocampal volume at the baseline to remove a part of the bias due to inter-subject variations. Results are presented in the (P-val.) columns of table I.

The P-values show first that the statistical power is higher using (SK_2) than (SK_1). This makes sense since the deformations at small scale are not biased by the deformations at large scale. Obviously, the methods (LSK_1) and ($\mathrm{SGK2}_1$) quantifying the deformations at a scale among others are more powerful than (SK_1) which measures deformations at all scales simultaneously. Interestingly, they also provide better distinctions than (SK_2), except for (LSK_1) with the average AOD. The key result is that ($\mathrm{SGK2}_1$) has a better discriminative power than (LSK_1) here. When comparing two shapes having feature differences at several scales simultaneously, it therefore appears that taking into account all feature differences simultaneously with a proper model is a serious alternative to a sequential approach. Additionally, this test shows that using a common value of g for images representing the same organ, pre-treated with the same pipeline and compared using the same kernel can lead to good results. Our strategy to tune the weight can then be used for an atlas creation or multiple comparisons by systematically using the same characteristic scales σ_n with the same weights a_n computed with a typical value of g for the compared images. Finally, our results also highlights the good behavior of our technique to extract the information at a scale of interest among others in non-segmented 3D MR images.

E. Measure of cortical folding

We apply now our technique to the longitudinal estimation of the early brain development out of 3D MR brain images. Our goal is to show the usability and potential of our algorithm on these images, so we limit our study to the comparison of two brains of 36.00 and 42.14 weeks of gestational age out of the same preterm infant. The images were acquired at the Hammersmith Hospital London (UK) with a spatial resolution of 0.85mm. Bias field correction was first performed using N3 [51] and the images were linearly aligned. Finally, in order to extract the brain grey matter, probabilistic segmentation of this structure was performed using the method of [52]. Our image comparisons focus on the extracted grey matter in the images referred by $I_{S,4}$ and $I_{T,4}$ in Fig. 8.

When comparing these images, we aim to quantify the growth of local structures like the sulci. The influence of the skull growth, expressed by a general growth of the brain, is also observed at a larger scale. It is then interesting to take into account feature differences at two scales simultaneously when quantifying the brain growth. Here, we used two characteristic scales: a large one ($\sigma_1 = 20$mm) and a small one ($\sigma_2 = 1.5$mm). We then registered $I_{S,4}$ onto $I_{T,4}$ using the large kernel σ_1 only **($\mathbf{LK}_3$)**, the small kernel σ_2 only **($\mathbf{SK}_3$)** and the sum of the kernels σ_1 and σ_2 with $a'_1 = 8a'_2$ **($\mathbf{SGK}_3$)**. The estimated initial momentum maps P_0 are first presented in Fig. 8. The final deformations of $I_{S,4}$ and the corresponding deformed grids are then presented with the amplitude of the deformation (AOD) from each point of $I_{S,4}$ in Fig. 9. Interestingly, for (SGK_3), we also separated the contribution of the large and small kernels. In Fig. 9 **($\mathbf{SGK1}_3$)** and **($\mathbf{SGK2}_3$)** therefore refer to the contribution of the large and small kernel respectively. Importantly, although the results are presented in a 2D slice, all comparisons were performed in 3D. The shape is then transformed in the 2D ROI but also across slices. This can be particularly noticed when observing carefully the deformed grids. Note finally that in the figures, the blue and red curves represent the surface of the grey matter in $I_{S,4}$ and $I_{T,4}$ respectively.

Src image $I_{S,4}$ (3D) **Src image $I_{S,4}$** **Trg image $I_{T,4}$**

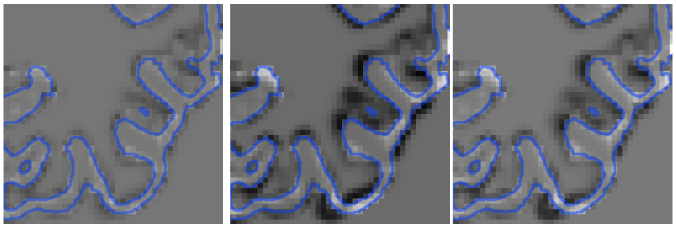

P_0 **SK$_3$** P_0 **LK$_3$** P_0 **SGK$_3$**

Fig. 8. **(Top)** Source image $I_{S,4}$ (centre) and target image $I_{T,4}$ (right). The region of interest on which the results are presented in this figure and Fig. 9 is shown in the red square on the left image. **(Bottom)** Initial momentum maps P_0 estimated using SK_3, LK_3 and SGK_3.

As presented in Fig. 9, the matching of the grey matter is accurate using (SK_3) and (SGK_3) while it is not the case using (LK_3). The deformation grids however highlight that the transformation estimated using (SGK_3) is clearly more regular than using (SK_3). Indeed, (SGK_3) registers properly feature differences observed at small scale but also those observed at large scale contrary to (SK_3). The deformation computed using (SGK_3) looks therefore more plausible.

In addition, the initial momentum maps of (SGK_3) and (LK_3) in Fig. 8 are more spatially regularized that the one of (SK_3). The initial momentum map of (SGK_3) is also more contrasted than the one of (LK_3). The interpretation of these results is particularly complex and will be addressed in future

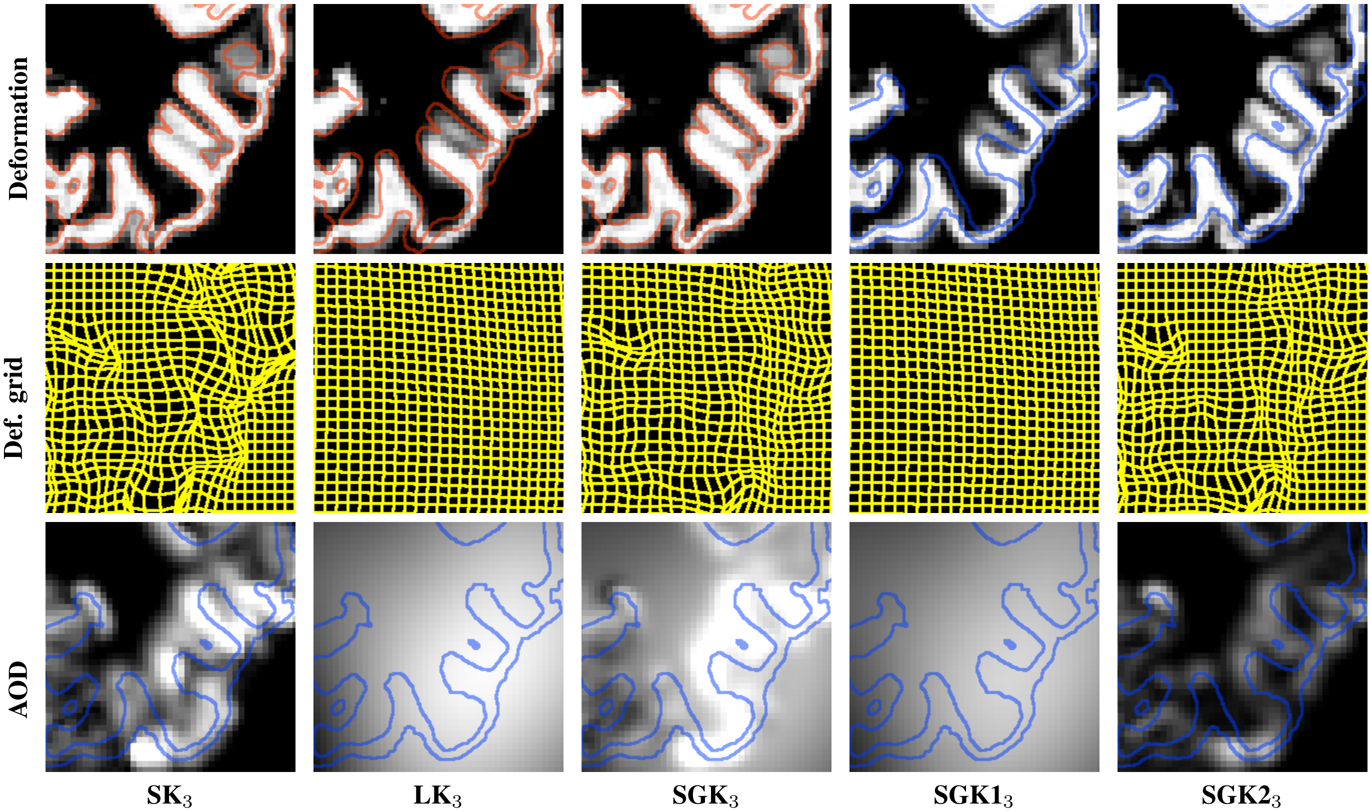

Fig. 9. **(Top)** Deformation of the source image $I_{S,4}$ on the target image $I_{T,4}$ at $t = 1$ using SK$_3$, LK$_3$, SGK$_3$, SGK1$_3$, and SGK2$_3$. **(Center)** Homogeneous grid deformed using the transformation of $I_{S,4}$ to $I_{T,4}$ at t=1 using the corresponding kernels. The initial grid has 1.5 mm of step size. **(Bottom)** Amplitude of the deformation (AOD) along the path of each voxel between t=0 and t=1 using the corresponding kernels. The grey levels are linearly sampled between 0 mm (black) and 3mm (white).

communications.

By observing the AOD in Figs. 9, the strategy (SGK2$_3$) appears as the best to quantify the growth of local structures like the sulci. (SK$_3$) and (SGK$_3$) indeed measure the deformations at small and large scale simultaneously while (SGK2$_3$) measures deformations at small scale with a minor influence of those observed at larger scale. Note that these deformations are quantified in millimeters, so their interpretation is natural even for a non-specialist. Remark finally that, even if the deformation (SGK2$_3$) of $I_{S,4}$ is only used qualitatively, it appears as a good complement to the AOD to interpret the results.

VII. CONCLUSION

In this paper, we have presented a practical and intuitive paradigm to integrate prior knowledge in the comparison of images having feature variations at one or several identified scales of interest. The user indeed defines a given number of scale of interest σ_n in millimeters and an automatic procedure helps him to tune the weights a_n associated with each σ_n. This approach is of particular interest in medical imaging since due to the increasing resolution of images, physiological phenomena occurring at several scales are more and more commonly observed. We have implemented our strategy in the context of LDDMM for 3D medical images to take advantage of the mathematical potential of this formalism, by including the prior knowledge in the deformation metric. In practice we have simply defined the kernels K associated to the metric as the sum of isotropic Gaussian kernel K_n, each Gaussian being parametrized by the standard deviation σ_n assimilated to a scale of interest. Interestingly, this strategy may also be developed in other fluid registration techniques by using similar smoothing kernels. Our tests have shown that this method estimates natural-looking deformations when registering images presenting feature variations at different scales simultaneously and preserves the mathematical properties of the LDDMM.

In addition, we have developed a strategy to extract quantitative information comparing the images at a given scale of interest among others. When comparing two images, all the pre-defined scales of interest are registered simultaneously and the amplitude of the deformations occurring at each scale are then quantified separately. It appears as an interesting alternative to classical coarse to fine approaches which register sequentially the images at large scale first and then at finer and finer scale. As shown in our tests, when the metric pertinently models the compared data, our method may indeed have a better statistical power than a coarse to fine technique to discriminate two image datasets with feature differences at a scale of interest among others. Interestingly, we have also developed a technique to illustrate qualitatively the meaning of the scale-dependent amplitude of deformations, by deforming the initial image at the corresponding scale of interest only. Note that the scale-dependent amplitudes of the deformations are expressed locally and in millimeters. The end-user can therefore interpret intuitively the results.

Future work will first consist in the validation of a multi-resolution approach, where the not only the scale of the kernel but also the image resolution will be treated. This will improve the time of computations, especially when registering large 3D images. More applications of our technique will also be carried out on MR cerebral images as well as on CT cardiac images. In particular, we will develop similarity metrics that are more adapted than the sum of square differences to treat the complex volumetric images observed in medical imaging, as initiated in [24]. In addition, making usable quantitatively and not only qualitatively the deformations representing the contribution of a kernel at a particular scale of interest will also be carried out. Developing the mathematical link between our method and [53] may be interesting for this purpose. Our work has finally two main methodological perspectives. The first one is to evaluate optimal parameterizations to perform inferential statistics in problem specific applications from large datasets. The second one is to develop and evaluate another formulation of the registration algorithm which works on the initial momentum maps directly. It would therefore strongly reduce the degrees of freedom of the problem and ensures geodesic properties of the deformations even before the convergence.

REFERENCES

[1] A. Klein, J. Andersson, B. A. Ardekani, J. Ashburner, B. Avants, M.-C. Chiang, G. E. Christensen, D. L. Collins, J. Gee, and P. Hellier, "Evaluation of 14 nonlinear deformation algorithms applied to human brain mri registration," *NeuroImage*, vol. 46, no. 3, pp. 786–802, July 2009.

[2] J. Feder, *Fractals*. NY Plenum Press, 1988.

[3] J. Gazit, D. Berk, M. Leunig, L. Baxter, and R. Jain, "Scale invariant behavior and vascular network formation in normal and tumor tissue. ," *Physical Review Letters*, vol. 75, pp. 2428–2431, 1995.

[4] L. Risser, F. Plouraboué, A. Steyer, P. Cloetens, G. Le Duc, and C. Fonta, "From homogeneous to fractal normal and tumorous micro-vascular networks in the brain," *Journal of Cerebral Blood Flow and Metabolism*, vol. 27, pp. 293–303, 2007.

[5] M. Sonka, V. Hlavac, and R. Boyle, *Image Processing, Analysis and Machine Vision*. Chapman and Hall, 1993.

[6] D. Marr, *Vision*. W. H. Freeman, 1982.

[7] P. J. Burt and E. H. Adelson, "The laplacian pyramid as a compact image code," *IEEE Transactions on communications*, vol. 31, no. 4, pp. 532–540, 1983.

[8] T. Lindeberg, *Scale-Space Theory in Computer Vision*. Kluwer Academic Publishers, 1994.

[9] J. Sporring, M. Nielsen, L. Florack, and P. Johansen, *Gaussian Scale-Space Theory*. Kluwer Academic Publishers, 1997.

[10] P. Perona and J. Malik, "Scale-space and edge detection using anisotropic diffusion," *IEEE Transactions on Pattern Analysis and Machine Intelligence*, vol. 12, no. 7, pp. 629–639, 1990.

[11] S. Mallat, "A theory for multiresolution signal decomposition: The wavelet representation," *IEEE Transactions on Pattern Analysis and Machine Intelligence*, vol. 11, no. 7, pp. 674–693, 1989.

[12] ——, *A Wavelet Tour of Signal Processing, Second Edition*. Academic Press Inc, 1999.

[13] M. Miller and L. Younes, "Group actions, homeomorphisms, and matching: A general framework," *International Journal of Computer Vision*, vol. 41, no. 1-2, pp. 61–84, 2001.

[14] A. Trouvé and L. Younes, "Metamorphoses through lie group action," *Foundations of Computational Mathematics*, vol. 5, no. 2, pp. 173–198, 2005.

[15] F. M. Beg, M. I. Miller, A. Trouvé, and L. Younes, "Computing large deformation metric mappings via geodesic flows of diffeomorphisms," *International Journal of Computer Vision*, vol. 61, no. 2, pp. 139–157, February 2005.

[16] L. Younes, A. Qiu, R. L. Winslow, and M. I. Miller, "Transport of relational structures in groups of diffeomorphisms," *Journal of Mathematical Imaging and Vision*, vol. 32, pp. 41–56, 2008.

[17] Y. L, A. F, and M. MI., "Evolutions equations in computational anatomy," *Neuroimage*, Nov. 2008.

[18] M. I. Miller, A. Trouvé, and L. Younes, "On the metrics and Euler-Lagrange Equations of Computational Anatomy." *Annual Review of Biomedical Engineering*, vol. 4, pp. 375–405, 2002.

[19] E. Haber and J. Modersitzki, "Cofir: coarse and fine image registration," *SIAM Real-Time PDE-Constrained Optimization*, pp. 37–49, 2007.

[20] J. Glaunes, "Transport par difféomorphismes de points, de mesures et de courants pour la comparaison de formes et l'anatomie numérique." Ph.D. dissertation, Université Paris 13, 2005.

[21] S. Marsland and C. J. Twining, "Constructing Diffeomorphic Representations for the Groupwise Analysis of Nonrigid Registrations of Medical Images." *IEEE Transactions on Medical Imaging*, vol. 23, pp. 1006–1020, 2004.

[22] S. Durrleman, X. Pennec, A. Trouvé, P. Thompson, and A. Ayache, "Inferring Brain Variability from Diffeomorphic Deformations of Currents: an integrative approach." *Medical Image Analysis*, vol. 12, pp. 626–637, 2008.

[23] S. Durrleman, X. Pennec, A. Trouvé, and A. Ayache, "Statistical Models of Sets of Curves and Surfaces based on Currents." *Medical Image Analysis*, vol. 13, pp. 793–808, 2009.

[24] D. Zhang, L. Risser, F. X. Vialard, O. Friman, L. Neefjes, N. Mollet, W. Niessen, and D. Rueckert, "Coronary motion estimation using probability atlas and diffeomorphic registration from cta." in *International Workshop on Medical Imaging and Augmented Reality (MIAR), Beijing - Lecture Notes in Computer Science*, 2010.

[25] L. Risser, F. X. Vialard, M. Murgasova, D. Holm, and R. D., "Large diffeomorphic registration using fine and coarse strategies. application to the brain growth characterization." in *International Workshop on Biomedical Image Registration (WBIR), Lübeck - Lecture Notes in Computer Science*, vol. 6204, 2010, pp. 186–197.

[26] L. Risser, F. X. Vialard, R. Wolz, D. Holm, and D. Rueckert, "Simultaneous fine and coarse diffeomorphic registration: Application to the atrophy measurement in alzheimer's disease." in *International Conference on Medical Image Computing and Computer Assisted Intervention (MICCAI), Beijing - Lecture Notes in Computer Science*, 2010.

[27] P. Dupuis, U. Grenander, and M. I. Miller, "Variational problems on flows of diffeomorphisms for image matching," *Q. Appl. Math.*, vol. LVI, no. 3, pp. 587–600, 1998.

[28] M. Miller, A. Trouvé, and L. Younes, "Geodesic shooting for computational anatomy," *J. Math. Imaging Vis.*, vol. 24, no. 2, pp. 209–228, 2006.

[29] M. Vaillant, M. Miller, A. Trouvé, and L. Younes, "Statistics on diffeomorphisms via tangent space representations," *Neuroimage*, vol. 23, no. S1, pp. S161–S169, 2004.

[30] M. F. Beg, P. A. Helm, E. McVeigh, M. I. Miller, , and R. L. Winslow, "Computational cardiac anatomy using mri," *Magnetic Resonance in Medecine*, vol. 52, no. 5, pp. 1167–1174, 2004.

[31] P. Helm, L. Younes, M. Beg, D. Ennis, C. Leclercq, O. Faris, E. McVeigh, D. Kass, M. Miller, and R. Winslow, "Evidence of structural remodeling in the dyssynchronous failing heart," *Circulation Research*, vol. 98, pp. 125–132, 2006.

[32] Y. Cao, M. I. Miller, R. L. Winslow, and L. Younes, "Large deformation diffeomorphic metric mapping of vector fields," *IEEE Trans. Med. Imaging*, vol. 24, no. 9, pp. 1216–1230, 2005.

[33] Y. Cao, M. I. Miller, S. Mori, R. L. Winslow, and L. Younes, "Diffeomorphic matching of diffusion tensor images," in *CVPRW '06: Proceedings of the 2006 Conference on Computer Vision and Pattern Recognition Workshop*, 2006, p. 67.

[34] M. Beg and A. Khan, "Symmetric data attachment terms for large deformation image registration," *Medical Imaging, IEEE Transactions on*, vol. 26, no. 9, pp. 1179–1189, 2007.

[35] G. Auzias, J. Glaunès, O. Colliot, M. Perrot, J.-F. Mangin, A. Trouvé, and S. Baillet, "Disco: a coherent diffeomorphic framework for brain registration under exhaustive sulcal constraints." in *International Conference on Medical Image Computing and Computer Assisted Intervention (MICCAI)*, 2009.

[36] B. B. Avants, C. L. Epstein, M. Grossman, and J. C. Gee, "Symmetric diffeomorphic image registration with cross-correlation: Evaluating automated labeling of elderly and neurodegenerative brain," *Medical Image Analysis*, vol. 12, pp. 26–41, 2008.

[37] S. R. Das, B. B. Avants, M. Grossman, and J. C. Gee, "Registration based cortical thickness measurement," *NeuroImage*, vol. 45, pp. 867–879, 2009.

[38] P. Lorenzen, M. Prastawa, B. Davis, G. Gerig, E. Bullitt, and S. Joshi, "Multi-modal image set registration and atlas formation," *Med Image Anal*, vol. 10, no. 3, pp. 440–451, June 2006.

[39] G. Hart, C. Zach, and M. Niethammer, "An optimal control approach for deformable registration," *Computer Vision and Pattern Recognition Workshop*, pp. 9–16, 2009.

[40] W. Crum, C. Tanner, and D. Hawkes, "Anisotropic multi-scale fluid registration: evaluation in magnetic resonance breast imaging," *Physics in Medicine and Biology*, vol. 50, no. 21, pp. 5153–5174, 2005.

[41] M.-C. Chiang, A. D. Leow, A. D. Klunder, R. A. Dutton, M. Barysheva, S. E. Rose, K. McMahon, G. I. de Zubicaray, A. W. Toga, and P. M. Thompson, "Fluid registration of diffusion tensor images using information theory," *IEEE Trans. Med. Imaging*, vol. 27, no. 4, pp. 442–456, 2008.

[42] V. Arsigny, O. Commowick, X. Pennec, and N. Ayache, "A log-Euclidean framework for statistics on diffeomorphisms," in *Proc. of the 9th International Conference on Medical Image Computing and Computer Assisted Intervention (MICCAI'06), Part I*, ser. LNCS, no. 4190, 2-4 October 2006, pp. 924–931, pMID: 17354979.

[43] M. Hernandez and S. Bossa, Matias N.and Olmos, "Registration of anatomical images using paths of diffeomorphisms parameterized with stationary vector field flows," *Int. J. Comput. Vision*, vol. 85, no. 3, pp. 291–306, 2009.

[44] T. Vercauteren, X. Pennec, A. Perchant, and N. Ayache, "Diffeomorphic demons: Efficient non-parametric image registration," *NeuroImage*, vol. 45, no. 1, pp. S61–S72, March 2009.

[45] J.-P. Thirion, "Non-rigid matching using demons," in *CVPR'96: Proceedings of the 1996 Conference on Computer Vision and Pattern Recognition (CVPR'96)*, 1996, p. 245.

[46] T. Vercauteren, X. Pennec, A. Perchant, and N. Ayache, "Symmetric log-domain diffeomorphic registration: A demons-based approach," in *MICCAI 2008*, 2008, pp. 754–761.

[47] J. Ashburner, "A fast diffeomorphic image registration algorithm," *NeuroImage*, vol. 38, pp. 95–113, 2007.

[48] F. X. Vialard, L. Risser, and C. Cotter, "Dimensionality reduction through geodesic shooting: Application to the comparison of volumetric 3d images." in *Annual Conference on Neural Information Processing Systems (NIPS - Submitted)*, 2010.

[49] N. Schuff, N. Woerner, L. Boreta, T. Kornfield, L. M. Shaw, J. Q. Trojanowski, P. M. Thompson, J. C. R. Jack, M. W. Weiner, and the Alzheimer's; Disease Neuroimaging Initiative, "MRI of hippocampal volume loss in early Alzheimer's disease in relation to ApoE genotype and biomarkers," *Brain*, vol. 132, no. 4, pp. 1067 – 1077, 2009.

[50] P. Yushkevich, B. . Avants, S. Das, J. Pluta, M. Altinay, C. Craige, and A. D. N. Initiative, "Bias in estimation of hippocampal atrophy using deformation-based morphometry arises from asymmetric global normalization: An illustration in adni 3 t mri data," *Neuroimage*, vol. 2, pp. 434–445, 2010.

[51] J. Sled, A. Zijdenbos, and A. Evans, "A nonparametric method for automatic correction of intensity nonuniformity in MRI data," *IEEE Transactions on Medical Imaging*, vol. 17, no. 1, pp. 87–97, 1998.

[52] *Construction of a dynamic 4D probabilistic atlas for the developing brain.*, 2010.

[53] M. Bruveris, F. Gay-Balmaz, D. Holm, and T. Ratiu, "The momentum map representation of images," arXiv:0912.2990v1 [nlin.CD].